

# Magnetic resonance imaging: Basic concepts and applications

P. Raghunathan and N. R. Jagannathan\*

*Magnetic resonance imaging (MRI) is a state-of-the-art imaging modality that has gained considerable attention in clinical medicine, particularly diagnostic radiology, because of its noninvasive nature and its sensitivity to the state of biological tissue. As an exquisite representation of the spatial distribution of mobile protons in the body, MRI presents the soft-tissue anatomical picture in any desired plane. This article reviews the historical development, the conceptual basics, and the diagnostic applications of various MRI techniques.*

ABOUT half a century ago, two independent groups of American scientists led by Edward Purcell<sup>1</sup> (Harvard University) and Felix Bloch<sup>2,3</sup> (Stanford University, USA) discovered hydrogen (proton) nuclear magnetic resonance (NMR) in solids and liquids, respectively. These discoveries led to the joint award of the Nobel prize to Bloch and Purcell in 1952.

NMR was initially used for spectroscopy and chemical structure elucidation, and towards the late 1960s, its use was demonstrated to produce signals from a live animal<sup>4</sup>. Several other research teams, including those of Cooke<sup>5</sup>, Hansen<sup>6</sup>, and Hazlewood<sup>7</sup>, began to publish further detailed studies on muscle in 1971. In the same year, observations on tissue specimens from animal tumours reported by Damadian<sup>8</sup> generated considerable interest in view of their medical diagnostic potential, and attempts by others to confirm and extend that work soon got underway, resulting in reports on rat hepatomas by Hollis and Saryan<sup>9</sup> and on a tumour in a living mouse by Weisman *et al.*<sup>10</sup> the following year.

The concept of magnetic resonance (MR) image formation evolved in the early 1970s, when Lauterbur produced two-dimensional proton images of a water sample<sup>11</sup>. This work soon led to imaging of other objects such as oranges, lemons and red pepper, then live animals and ultimately humans<sup>12,13</sup>. MRI thus came into being as a safe, noninvasive diagnostic technique in biomedical research<sup>14</sup> and clinical practice<sup>15</sup>.

The purpose of this article is to acquaint the practitioner of chemical and biological sciences with the fundamentals of this magnetic resonance method. Although a knowledge of quantum mechanics of spin particles, electromagnetic theory and radiofrequency electronics, and computational techniques is necessary for a deep

and thorough understanding of MRI, in this article such topics have been deliberately circumvented in the interests of a clearer overview.

## Basic phenomenon – magnetization

How does one manipulate tiny magnetic nuclei to obtain a three-dimensional image of the human organ? The first step is to magnetize the tissue.

The nucleus of hydrogen is not only positively charged but also has the inherent property of a 'spin' (Figure 1 *a*), and a spinning electric charge generates a magnetic field (Figure 1 *b, c*). The proton is therefore conceptualized as a spinning 'nuclear magnetic dipole' and depicted as a vector parallel to the axis of spin. In a neutral environment the billions of protons in bulk matter such as tissues, for example, have their magnetic moment vectors randomly oriented, averaging the nett bulk magnetization to zero. In the presence of an applied static magnetic field ( $B_0$ ), however, these dipoles 'precess', or execute a wobbling motion delineating the surface of a cone, analogous to the familiar example of a spinning top wobbling in the earth's gravitational field.

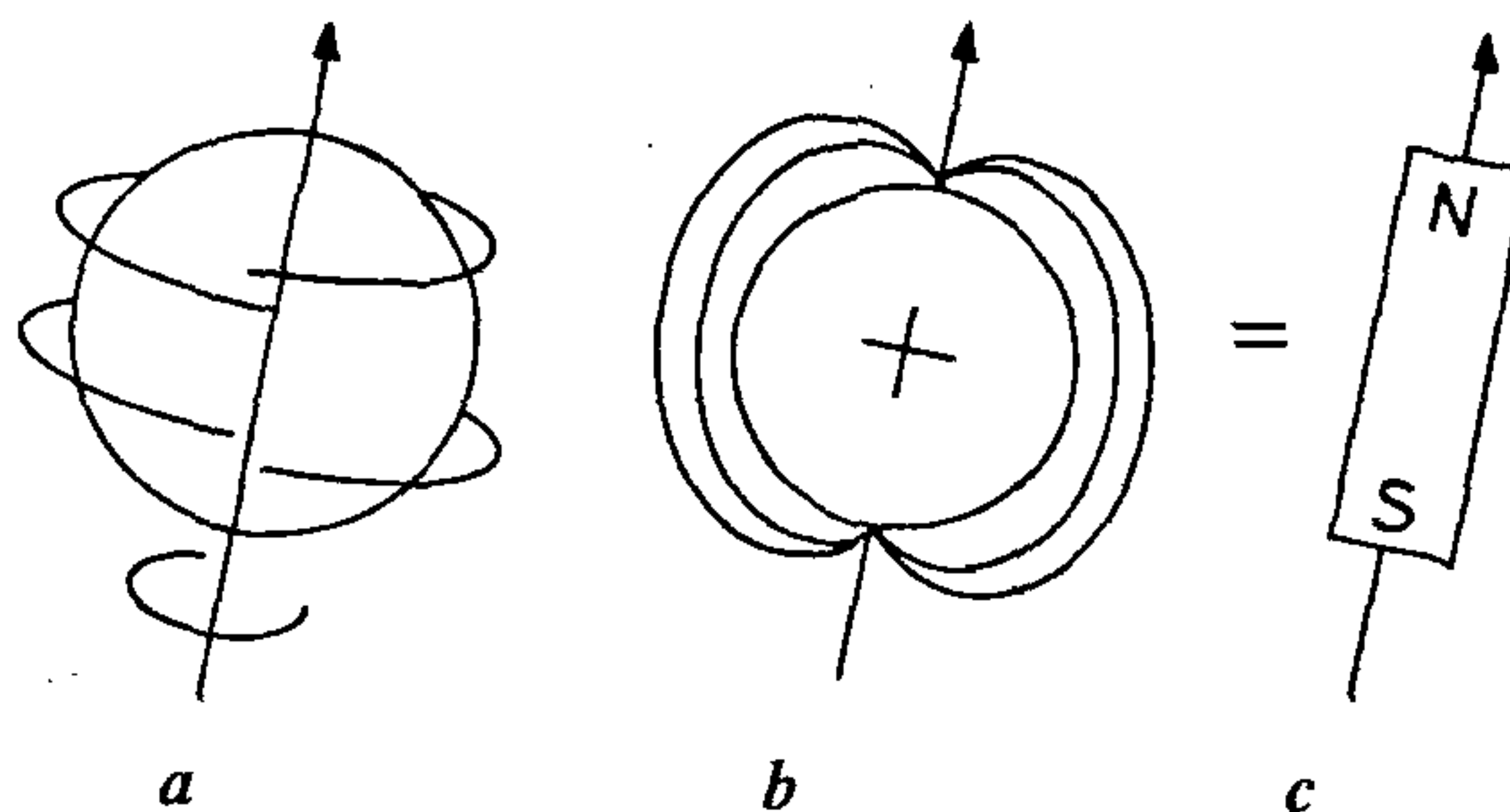


Figure 1. *a*, The concept of nuclear 'spin'; *b* and *c*, The spinning nucleus viewed as a tiny magnet.

P. Raghunathan and N. R. Jagannathan are in the Department of NMR, All India Institute of Medical Sciences, Ansari Nagar, New Delhi 110 029, India

\*For correspondence

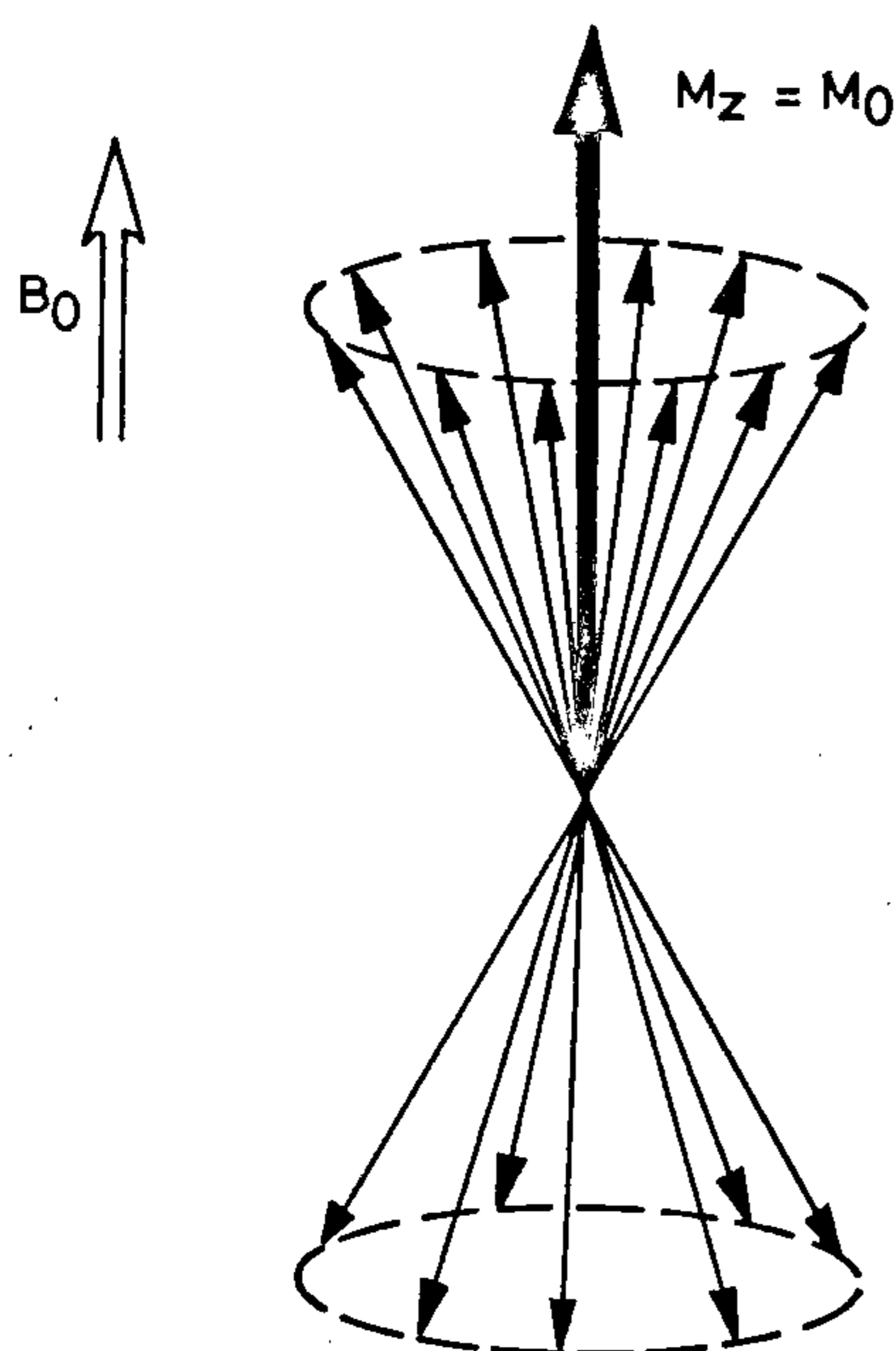


Figure 2. Vector representation of nuclear magnetization in the presence of an applied  $B_0$  field.

Macroscopically, the precessing proton dipoles tend to get reoriented in one of the two directions, namely, with the precessional cone axis aligned either parallel or antiparallel to the  $B_0$  direction which is conventionally defined along the Cartesian  $z$  axis (Figure 2). The parallel alignment of the cone axis corresponds to the low-energy state of the proton population while the other alignment, which requires excess energy to oppose the  $B_0$  field, corresponds to the high-energy state. Basic considerations of thermal equilibrium dictate that, for protons at the body temperature (310 K), there is a very slight population excess – about seven per million – in the lower energy state. It is this small population excess which gives rise to the nett longitudinal magnetization,  $M_0$ , in the direction of  $B_0$  (Figure 2).

The aforementioned creation of  $M_0$  in the tissue under study is the first step in extracting imaging information exploiting the nuclear spins. Whereas many atomic

nuclei have the property of spin, current MR imagers used in biomedicine focus mainly on the nuclei of hydrogen occurring in the form of water or lipids. Theoretically, and in practice, it is possible to observe NMR signals from other nuclei occurring in biosystems, such as phosphorus ( $^{31}\text{P}$ ) and sodium ( $^{23}\text{Na}$ ). However, these nuclei occur in substantially lower concentrations (Table 1) and are therefore difficult to be imaged.

### The phenomenon of resonance and the production of an electrical signal

To generate a measurable signal from the magnetized object, the concept of a vector precession model is used to define two important quantities underlying the basic physics of MR imaging, namely, the Larmor frequency ( $\omega$ ) and the phase ( $\phi$ ). The former refers to the frequency of precessional motion of the nuclear spins about the applied field,  $B_0$ . The Larmor frequency is proportional to the strength of  $B_0$ , namely

$$\omega = \gamma |B_0|, \quad (1)$$

where  $\gamma$ , the magnetogyric ratio, is a fundamental constant typifying the particular spin species (see Table 1). For hydrogen nuclei subjected to commonly employed  $B_0$  field strengths of the order of a Tesla (1 Tesla = 10,000 gauss), one sees that the Larmor frequency lies in the radio-wave region of the electromagnetic spectrum. The precessing vectors shown in Figure 2 are randomly phased with respect to each other and could therefore be more appropriately called 'phasors'. Phase ( $\phi$ ) may be defined as the angle through which the spinning nucleus precesses in a given time. Indeed,  $\phi$  is the temporal integral of the Larmor frequency,

$$\begin{aligned} \phi &= \int_0^t \omega \, dt' \\ &= \gamma \int_0^t B_0 \, dt', \text{ from equation (1).} \end{aligned} \quad (2)$$

To induce resonance and observe a signal, a radiation of appropriate frequency  $\omega$  is needed, which is in the radiofrequency (RF) range. RF radiation is basically an electromagnetic oscillation possessing both electrical and magnetic field vectors which are mutually perpendicular to each other. Therefore, RF radiation could be applied suitably to impose a second magnetic field ( $B_1$ ) pointing perpendicular to  $B_0$ . In the presence of an RF magnetic field ( $B_1$ ) which is tuned to rotate at the precession frequency of the nuclei, the phenomenon of resonance occurs, i.e. by virtue of this frequency 'match', RF energy will be absorbed from the  $B_1$  field by the precessing nuclei and they will be promoted to the higher energy state so that  $M_z$ , the magnetization

Table 1. NMR properties of medically important nuclei

Nucleus	Magnetogyric ratio (MHz/Tesla)	Relative abundance (%)	Relative sensitivity
$^1\text{H}$	42.58	99.98	1.00
$^7\text{Li}$	16.54	92.58	0.27
$^{13}\text{C}$	10.71	1.11	0.016
$^{19}\text{F}$	40.05	100.00	0.83
$^{23}\text{Na}$	11.26	100.00	0.093
$^{31}\text{P}$	17.23	100.00	0.066

component along  $z$ , is reduced<sup>16</sup>. Since  $B_0$  is a rotating magnetic field, it is customary to invoke a 'freeze-frame' picture by using a set of axes that rotate about the  $z$  axis at precisely the Larmor frequency in the  $x'y'$  plane (the primes indicate rotating frame axes), and thereby to define  $B_1$  to lie along the  $x'$  axis. In this rotating frame representation,  $B_1$  flips  $M_z$  away from the  $z$  axis by an angle  $\theta$  and  $M_z$  is reduced to  $M_z \cos \theta$ . Simultaneously, a transverse component of the magnetization develops along the  $y'$  axis, proportional to  $\sin \theta$ . The 'flip' angle depends on the value of  $B_1$  and the duration ( $\tau$ ) for which this field is applied:

$$\theta = \gamma |B_1| \tau. \quad (3)$$

Since  $B_1$  is applied as a 'pulse' or 'burst',  $\tau$  usually represents a short period, and hence the concept of a  $90^\circ$  pulse, which is one that produces maximum  $M_y$ , and zero  $M_z$ . Similarly, a  $180^\circ$  RF pulse is obviously one that produces no  $M_y$ , but  $-M_z$ , i.e. an inversion of the nuclear magnetization. The  $M_y$  magnetization produced by the  $90^\circ$  RF pulse and rotating freely (at the Larmor frequency) in the transverse plane is potentially a generator of electricity. A receiver coil placed appropriately in the transverse plane, and tuned to the Larmor frequency, will therefore receive an electrical signal voltage proportional to the  $M_y$  component.

Excitation of the spin system by the  $B_1$  pulse has two important effects: it promotes some spins to the higher energy state, and it also forces a phase coherence among the spins and causes a summation of their magnetic moments in the  $x'y'$  plane. When the  $B_1$  pulse is switched off, there is a progressive loss of phase coherence among the spins due to inhomogeneous intra- and inter-molecular magnetic fields, and the spin vectors 'fan out'. Since the signal picked up by the receiver coil is proportional to the phase-coherent component of the transverse magnetization, the signal following the brief RF pulse decays in time. Such a decaying resonance signal is called a 'free induction decay' (FID).

### The Fourier transform relationship between the time and frequency domains

Assuming a uniform  $B_0$  field and the presence of only a single chemical entity in the sample (say, hydrogens in water), the FID is a single exponentially decaying signal, whose frequency component is just the resonance frequency (see Figure 3a). If the sample contains groups of nuclei in different local magnetic fields (and therefore having different precessional frequencies), then the signal will be more complex (Figure 3b). It is then necessary to analyse this time-domain signal,  $f(t)$ , into its individual frequency components,  $F(\omega)$ . This can be accomplished by the Fourier transformation (FT),

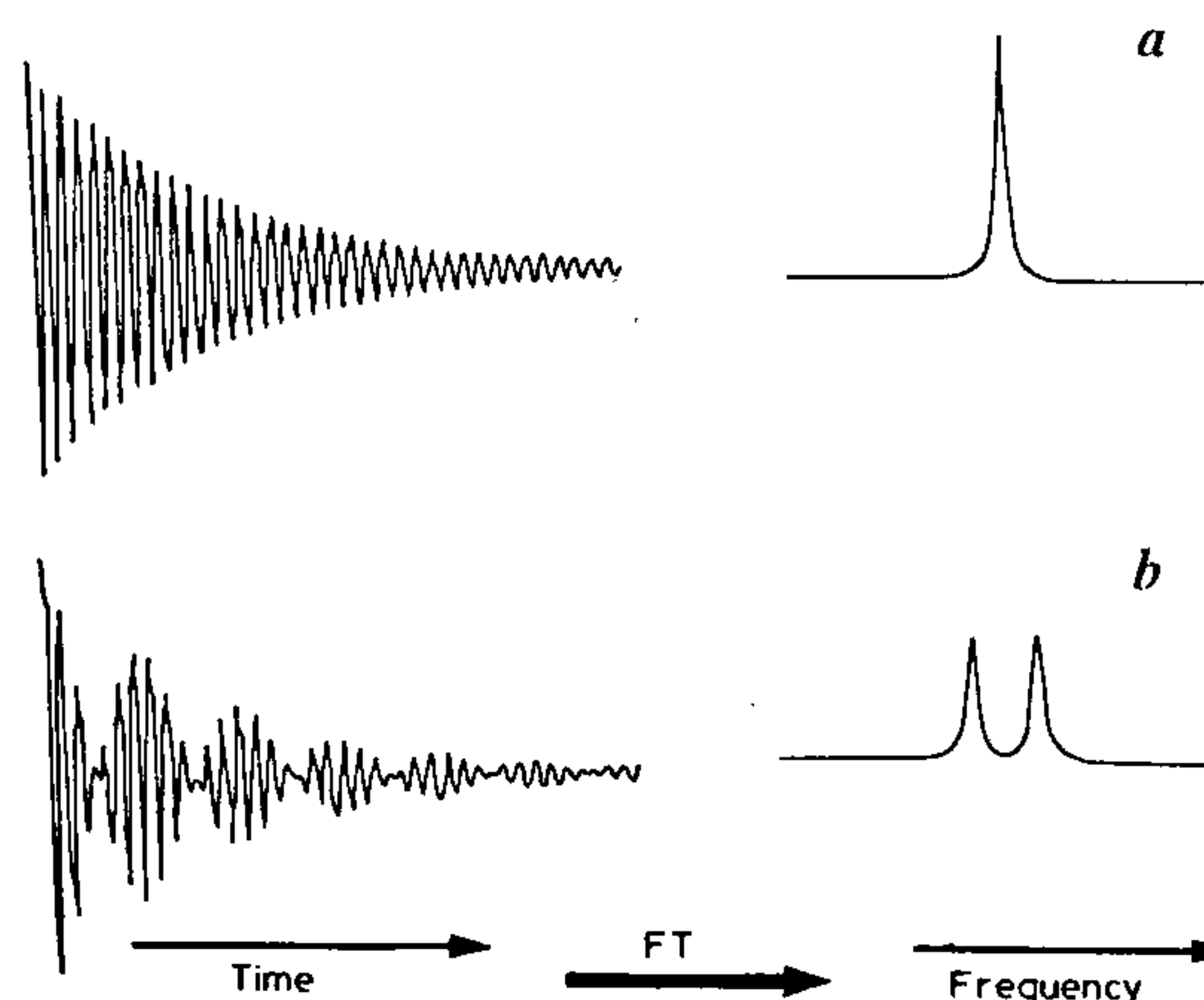


Figure 3a, b. Examples of free induction decays (FID) and their Fourier transforms (FT). a, A single decaying FID and its frequency domain spectrum after FT; b, Two decaying FIDs and their frequency domain spectrum after FT.

$$F(\omega) = \int_{-\infty}^{\infty} f(t) e^{-i\omega t} dt. \quad (4)$$

In common practice, the time-domain signal voltage is first digitized electronically, and then Fourier-transformed to the frequency domain by means of a discretized version of equation (4). For a detailed description of FT in NMR, the reader is referred to Shaw<sup>16</sup>.

### Relaxation

Subsequent to excitation by the RF pulse, the precise way in which the nett magnetization of the spins relaxes back to the original state of thermal equilibrium gives important information about the characteristics of the tissues being imaged. There are two basic mechanisms that drive relaxation, namely, (a) transverse (spin-spin) and (b) longitudinal (spin-lattice). Both may be thought of as first order or exponential processes, i.e. the effects of magnetization decay due to these processes can be characterized by

$$M \propto \exp(-t/T), \quad (5)$$

where  $T$  defines either the spin-spin or spin-lattice relaxation time constant. Moreover, the two processes occur synchronously, but for convenience they are discussed separately.

### Transverse or spin-spin relaxation

We have stated earlier that instantaneously after the  $90^\circ$  RF pulse, the nett magnetization is transverse to the  $B_0$

field. All the nuclei making up this transverse magnetization are momentarily phase-coherent, and their combined magnetic moments register the maximum FID signal. These magnetic moments interact with one another and cause local deviations of the magnetic field, resulting in some of the nuclei precessing at different rates. This effect becomes more marked with time, until eventually there is no longer any nett magnetization in the transverse plane indicating that the spins have reached a state of internal equilibrium amongst themselves in the rotating frame. This is known as loss of phase coherence or dephasing. The time characterizing this dephasing process is known as spin-spin relaxation time,  $T_2$ . From the exponential relationship shown in equation (5), we see that one  $T_2$  interval is the time it takes for 63% of the coherent transverse magnetization to be lost.

Furthermore, in actual practice, even with modern magnet design, one does not achieve a completely homogeneous  $B_0$  field, and this means that dephasing occurs quicker than it would if  $B_0$  were completely homogeneous. The time constant characterizing the loss of the transverse magnetization under these circumstances is denoted by  $T_2^*$ . The effects of  $B_0$  inhomogeneity can be ruled out by using a special RF pulse sequence when performing an MR scan.

A pulse sequence is a series of timed RF pulses which are repeated many times at time intervals  $TR$  during a single data acquisition in order to obtain sufficient image information. The pulse sequence which leads to images with a sensitivity to  $T_2$  (dubbed as ' $T_2$ -weighted images') is called a spin-echo sequence. This shall be described later and we merely emphasize at this point that spin-spin relaxation provides a good source of soft-tissue contrast in MR images.

### *Longitudinal or spin-lattice relaxation*

The second process occurring after RF excitation of the nuclei is the tendency of the nuclei, and therefore of the nett magnetization, eventually to return to the original bulk ('lattice') thermal equilibrium by re-aligning with  $B_0$ . This happens because the RF energy absorbed by the nuclei is lost as heat to the surrounding bulk; without that extra energy the nuclei are unable to oppose  $B_0$ , and consequently re-align with it. The nett  $M_0$  magnetization is then fully restored along the longitudinal axis.

Longitudinal relaxation has a time constant  $T_1$ , one  $T_1$  interval being the time taken for the tissue to recover 63% of its  $M_0$  magnetization. This is typically hundreds of milliseconds for protons in human tissue. It is important to realize that longitudinal and transverse relaxation occur together, and that different tissues have different spin-lattice and spin-spin relaxation features depending on their fluidity.  $T_2$  is always shorter than or equal to  $T_1$ .

An interesting point to note is that if a second  $90^\circ$  RF excitation pulse is switched on after an interval  $TR$  which is less than or even equal to  $T_1$ , the detectable signal produced by the second pulse ( $\propto M_z$ ) will be less than that produced by the first by  $[\exp(-TR/T_1)]$ , since  $M_z$  has not relaxed to its full value. On application of a series of  $90^\circ$  RF pulses, a 'steady state' is achievable, and the signal is then given by

$$M_z = M_0 [1 - \exp(-TR/T_1)]. \quad (6)$$

This effect is called 'saturation', and is the basis for  $T_1$  contrast in short- $TR$  images<sup>15</sup>.

### **Spin echo**

The RF sequence for producing a spin echo uses a  $90^\circ$  pulse followed by a  $180^\circ$  pulse. A diagrammatic vector representation of the spin echo phenomenon is shown in Figure 4. We start with the equilibrium magnetization aligned along  $z'$  of the rotating coordinate system (Figure 4 a). At time  $t = 0$  immediately following the  $90^\circ$  RF pulse, the nett magnetization is tipped over into the  $x'y'$  plane, and all the contributing magnetization is tipped over into the  $x'y'$  plane, and all the contributing spins are phased (spinning in synchrony) to produce a resultant magnetization along  $y'$  (Figure 4 b). However, because of magnetic field inhomogeneities, some of these spins will precess at a faster rate and some others at a slower rate, resulting in a gradual loss of phase coherence and a consequent loss of signal. The situation at the instant of time  $t = TE/2$  is shown in Figure 4 c.

At this exact time  $t = TE/2$ , application of the  $180^\circ$  pulse reverses the phase, or the relative movement, between the vectors. The 'fast' vectors now lag behind the 'slow' ones (Figures 4 d, e). This phase reversal results in a gradual rephasing. At time  $t = TE$  after the initial  $90^\circ$  pulse, rephasing is completed with the nett transverse magnetization appearing along  $-y'$  axis. In other words, the effects of magnet inhomogeneities have now been completely refocused, and the 'spin echo' signal is produced (Figure 4 f). The amplitude of this echo signal is seen to be attenuated by the factor  $\exp(-TE/T_2)$  due to the irreversible dephasing caused by the  $T_2$  relaxation process, but adverse effects of  $B_0$  inhomogeneities have been eliminated.

### **Production of an MR image**

Any image in general has to have spatial information content, either in two or three dimensions, and we therefore consider how spatial information can be encoded onto the resonating spins. Images produced in MRI represent slices in various preselected planes through the patient's body. Each slice of tissue, actually composed of numerous volume elements or voxels, is displayed in a two-dimensional form on a monitor or a photographic

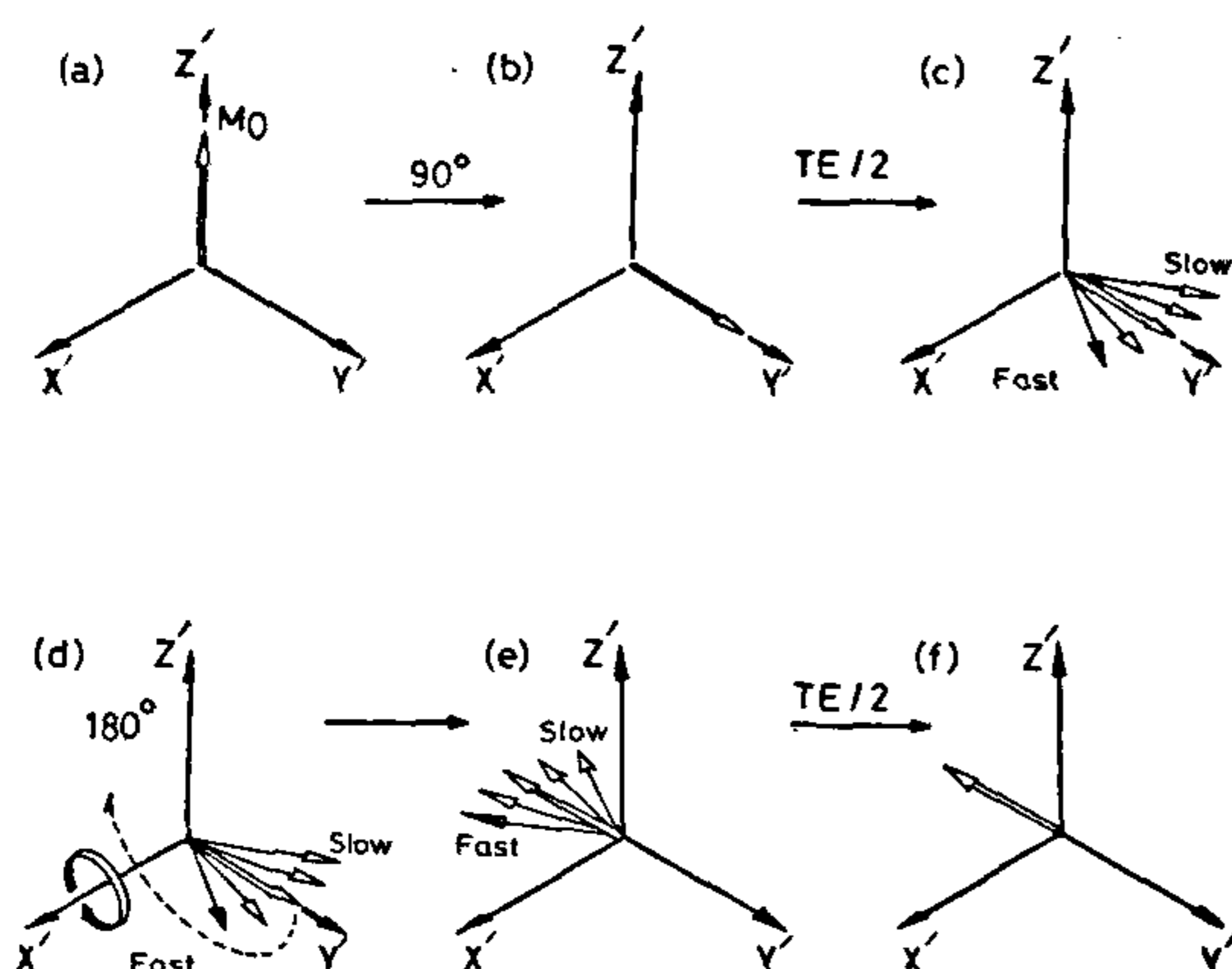


**Figure 4.** Diagrammatic vector representation of the spin-echo phenomenon. See text for details.

film. The voxels are then represented by an array of picture elements or pixels. Using appropriately wound current-carrying coils, if a magnetic field gradient is applied which alters the strength of  $B_0$  across the excited slice, then the protons will resonate at a frequency according to their *position* along the applied gradient. The signal detected will contain a range of frequencies and amplitudes, the frequencies corresponding to the range of  $B_0$  field strengths, and amplitudes to the number of protons contributing to the signal brightness (intensity).

The key to spatial encoding of spins is thus the use of linear magnetic field gradients, and this was originally proposed by Lauterbur<sup>11</sup>. When a linear gradient,  $G_x$  (in units of field strength per unit distance), is applied along the  $X$  direction, a linear increase in  $B_0$ , and hence in the Larmor frequency,

$$\omega = \gamma (B_0 + XG_x), \quad (6)$$

is created along the  $X$  coordinate in the sample. For the simple case of a phantom made up of two tubes of water placed at  $X_a$  and  $X_b$  along the  $X$ -direction (Figure 5), application of  $G_x$  causes the water protons in each tube to resonate at a different Larmor frequency, namely,

$$\omega_a = \gamma (B_0 + X_a G_x), \quad (7a)$$

$$\omega_b = \gamma (B_0 + X_b G_x), \quad (7b)$$

and we see that the two frequencies have become spatially encoded. The FT NMR spectrum will consist of two lines with a frequency separation of  $[\gamma(X_a - X_b)G_x]$ . This spectrum, however, is a simple one-dimensional projection of the two-tube water phantom onto the  $x$ -axis.

For an image reconstruction, it is obviously necessary to have more information than a single projection. A

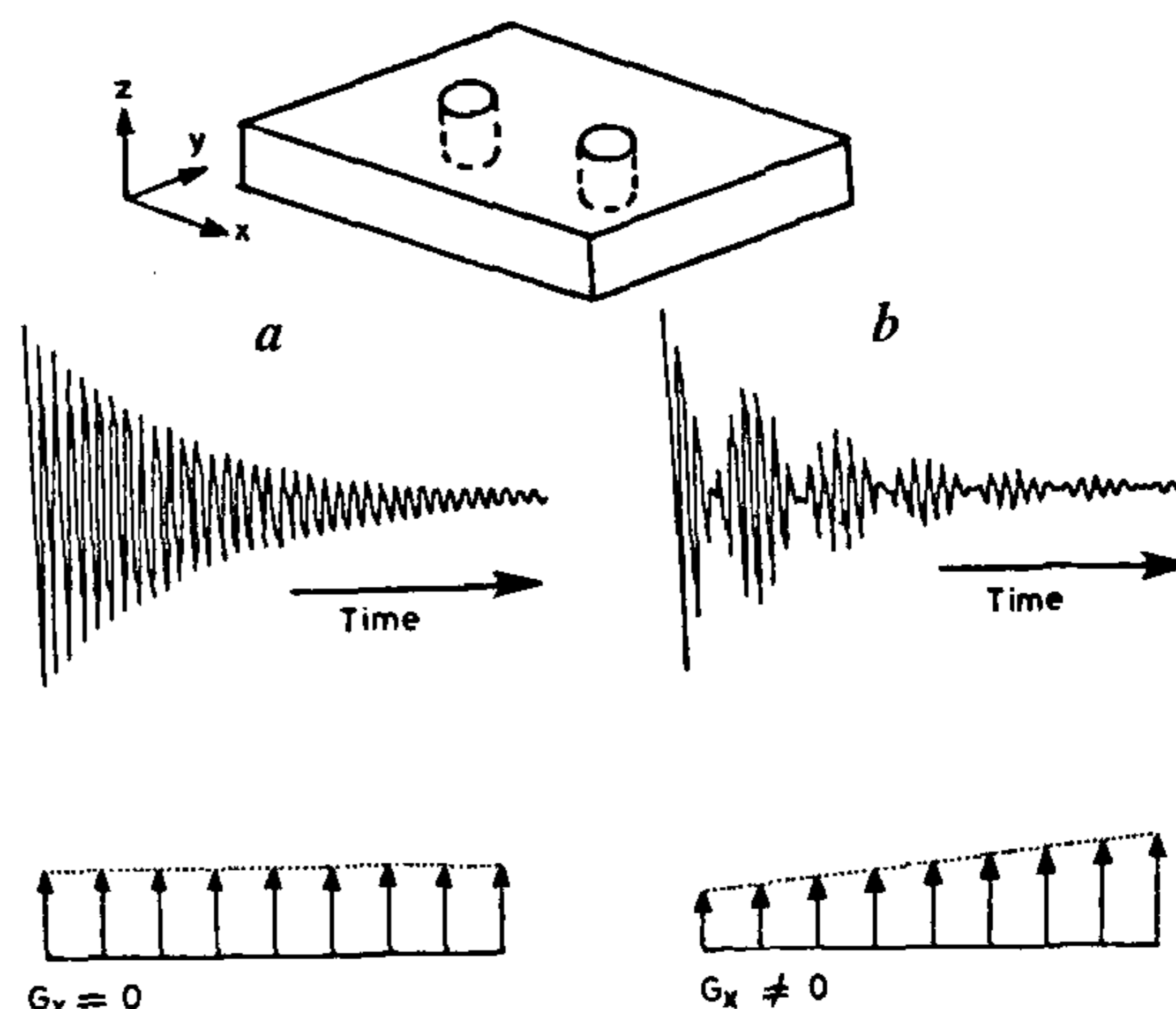


**Figure 5a, b.** Frequency encoding of two tubes of water for producing an image. *a*, With no field gradients ( $G_x = G_y = G_z = 0$ ) both samples sense the same  $B_0$  field resulting in a single free induction decay; *b*, In the presence of a gradient ( $G_x \neq 0$ ), the two sample tubes sense different fields, resulting in a complex FID consisting of two frequencies.

linear  $Y$ -gradient ( $G_y$ ) will yield a second projection, which would be adequate for the simple case of two tubes, but in general more information is necessary to produce an image. In the original approach of Lauterbur<sup>11</sup>, a vectorial combination of  $X$  and  $Y$  gradients was used to produce a number of 'ray' projections and to reconstruct an image by filtered back-projection methods used in X-ray computed tomography (CT). However, such 'projection-reconstruction' methods are very sensitive to motion artifacts and  $B_0$  inhomogeneities and are rarely used nowadays in MRI.

The currently-used imaging methods fall in the category of 'Fourier imaging', and exploit properties of Fourier transforms, as shown by Ernst *et al.* (see ref. 18). Collecting a series of data points in the presence of a  $G_x$  gradient (which is called a 'readout' gradient), frequency-encodes the signal and produces, following FT, a series of spatially-defined image points. To define a two-dimensional image, spatial information about the  $y$ -axis must also be encoded on to the signal. This is done by recalling the 'phase' property of the resonant nuclear spins, equation (2), and writing

$$\phi = \gamma Y \int_0^t G_y(t') dt'. \quad (8)$$

The above equation shows that the accumulated phase scales with  $\gamma Y G_y$ , where  $Y$  is the second spatial dimension we are seeking to encode.

Thus, if the phase-encoding  $G_y$  gradient is left on for a time  $t$ , the relative phase of a signal depends on  $G_y$  and its position ( $Y$ ). The signal at the start of the data col-

lection period in the presence of the readout ( $G_x$ ) gradient, which immediately follows the phase-encoding period, is thus phase-shifted by an amount depending on the position of spins with respect to the  $Y$ -gradient. If the readout is repeated with a different value of  $G_y$  (or as was originally done by Ernst for a different duration of the same  $G_y$  gradient<sup>17,18</sup>), then a new 'view', i.e. a new set of  $n$  time-domain points, which differ from the first set in their initial phases, is obtained. Repeating the procedure for  $m$  equal increments of  $G_y$  produces a matrix of 'raw data' consisting of  $m$  rows (time variable) and  $n$  columns (phase variable). A 2-dimensional FT, both along the rows and down the columns, produces a map or image of intensity over the plane defined by the two axes along which the two gradients are used.

Application of the third gradient,  $G_z$ , perpendicular to the imaging plane determines how a slice is first selected and excited in a three-dimensional object for subsequent imaging. It is possible to choose millimeter-thin slices, since slice thickness is related directly to the RF pulse bandwidth and reciprocally to the value of  $G_z$ . Further, in the gradient hardware of an MRI system, each gradient-coil pair is so defined that its 'zero gradient' point coincides exactly with the isocentre of the main magnet. It is possible, therefore, to excite an off-centre slice by changing the centre-frequency of the RF pulse bandwidth. Finally, the narrow bandwidth RF pulse, if properly 'shaped', could lead to the near-ideal 'rectangular' slice profile. This is achieved, for example, by using a mathematical function called a 'sinc' [ $\sin(x)/x$ ] to modulate the RF pulse waveform. The underlying concept here is that the Fourier transform of the sinc function is a rectangle.

The basic algorithm for MR image generation for acquiring a set of 2-D axial images<sup>18</sup> may now be set forth:

- selection of a planar axial slice applying  $G_z$  and simultaneous excitation of the spins in this planar slice by a shaped RF slice of appropriate bandwidth;
- phase-encoding by applying  $G_y$  of a certain amplitude for a fixed time;
- application of the  $G_x$  (read-out) gradient and collection of  $n$  points of raw-data;
- a stepped incrementation of  $G_y$  amplitude and repetition of the previous three steps  $m$  times; and
- 2-D Fourier transformation of the raw data to produce an  $m \times n$  image, the collection of a larger number of data points corresponding to 'fine-graining' and therefore a better-resolved image.

Although the number of phase-encoding steps determine the  $y$ -axis resolution for the acquired image, it is this number which also determines the total MR imaging time (along with  $TR$  and the number of signal averages (NSA)). It is also to be noted that if an anatomical plane other than the axial, such as the coronal or the sagittal,

is to be imaged, the function of each of the field gradients above will be defined accordingly<sup>15</sup>.

### Multi-slice imaging

In simple 2D-FT imaging, slices are activated one at a time over a  $TR$  period, and considerable time is wasted in waiting for the spins to relax in between excitations. One can accelerate image acquisition significantly by a slice-multiplexing approach by using the 'dead time' between the end of data collection and the next slice-selective pulse. Slice 1 is excited and, once data collection from this slice is completed, slice 2 is excited and so on until the time ( $TR$ ) required for image contrast has elapsed and slice 1 is returned to. The end of the data collection period is basically dictated by the  $TE$  of the last echo. Very roughly, since the gain in efficiency scales with the  $TR/TE$  ratio, we have an order of magnitude improvement in the imaging time here.

### $k$ -Space and fast-imaging sequences

As noted earlier, the raw image appears as a matrix made up of a number of rows of data points, with each row corresponding to a single phase-encoding step and each point along that row corresponding to a different spatial phase (as determined by the frequency-encoding gradient). This 2-D matrix is known as  $k$ -space, and it is the different methods of filling  $k$ -space which are utilized in fast imaging techniques.

The central portion around the origin of  $k$ -space (which would correspond to the smallest values of phase-encoding gradients) gives rise to the intensity pattern of the image. The more peripheral portions (corresponding to higher phase-encoding gradient values) contribute to the resolution of the image.

In conventional 2D-imaging, one line of  $k$ -space, called a 'view', is collected for each phase-encoding step during acquisition and, therefore, the total acquisition time will be equal to [number of phase-encoding steps  $\times$  NSA  $\times$   $TR$ ]. Since  $k$ -space possesses the property of conjugate symmetry, 'half-Fourier imaging' utilizes this fact and collects a little over half of the  $k$ -space data and computes the remaining half as a mirror image. By halving the number of phase-encoding steps in this manner, the total acquisition time is halved. The trade-off here, of course, is that the resultant images suffer from a reduction in signal-to-noise ratio by 2, and the technique is also more susceptible to motion and  $B_0$  inhomogeneities.

There is a host of other methods<sup>19-21</sup> available for the rapid build-up of raw data in  $k$ -space. Pulse sequences have been developed which use spiral, diagonal, sinusoidal and rectangular trajectories to fill up as much  $k$ -space as possible per unit time. The ultimate in these

sequences is echo planar image (EPI), pioneered by Mansfield<sup>22</sup>, that allows a single image to be acquired in one  $TR$ . The requirements imposed upon the hardware to produce rapidly oscillating gradients, together with the complex image reconstruction techniques involved, make many of these alternative scanning techniques suitable only for research at the present time.

There are numerous reasons for acquiring data quickly: to minimize patient discomfort, to minimize movement/respiration artifacts, and to improve patient throughput. There is also the possible application to dynamic studies of organs, such as imaging various phases of the cardiac cycle. In this context, a brief mention about gradient-echo (GE) based techniques is essential. GE techniques incorporate a whole family of different pulse sequences which rely on a reduced flip angle (equation (3)) and short  $TR$ . These have been developed to provide more rapid acquisition – in seconds rather than in minutes required for the more conventional acquisition methods.

In conventional SE imaging, a  $90^\circ$  pulse is used, followed by a  $180^\circ$  refocusing pulse to form the echo, whereas the GE pulse sequence uses pulse flip angles of less than  $90^\circ$ . The  $180^\circ$  rephasing pulse is no longer used; it is replaced by reversal of the magnetic field gradient which refocuses the signal in the transverse plane, hence the name 'gradient echo'. More than one RF pulse is of course used in a GE sequence, and this has the result of a stimulated spin echo formation which combines with the FID produced by each RF pulse to form the echo.

GE sequences are given different acronyms by the different machine manufacturers. Basically the sequences can be divided into three categories: (i) steady state echoes, (ii) spoiled gradient echoes and (iii) contrast-enhanced gradient echoes. Table 3 lists the different commercial acronyms by which these sequences are known and the contrast they produce. For further details regarding the various GE-based image sequences, the reader is referred to Wehrli<sup>23</sup>.

### MRI applications: A brief survey

The MR image corresponds not only to tissue density, as in the case of images obtained by X-ray, CT scanning or ultrasound, but is rather an image of tissue chemistry, in fact a physicochemical blueprint, showing structures in terms of hydrogen nuclei with a given set of relaxation properties. In future, the image may be changed to reflect the chemistry based on other vital nuclei as well<sup>24,25</sup>.

It will perhaps be easy to appreciate at this point that the  $T_1$  and  $T_2$  characteristics (see Table 2) discussed above are in fact responsible for MRI signals of one region of the body differing in intensity from those of another region as illustrated in Figure 6. It is clear that

**Table 2.** Approximate relaxation times  $T_1$  and  $T_2$  at a field strength of 1.5 Tesla for various tissues together with the relative values of mobile hydrogen nuclei (spin density)

Tissue	$T_1$ (ms)	$T_2$ (ms)	Relative spin density (%)
Fat	260	80	98
Liver	490	40	91
White brain matter	780	90	100
Gray brain matter	920	100	94
Spleen	780	60	92
Skeletal muscle	860	50	100
Heart muscle	860	60	100

**Table 3.** Types of gradient echo sequences

Category of GE sequence	Commercial acronyms	Contrast possible
Steady state	GRASS, FISP, T2FFE	$T_2^*/T_1$
Spoiled	SPGR, FLASH, T1FFE	$T_1$ , proton density
Contrast-enhanced	CE-FAST, PSIF	$T_2$

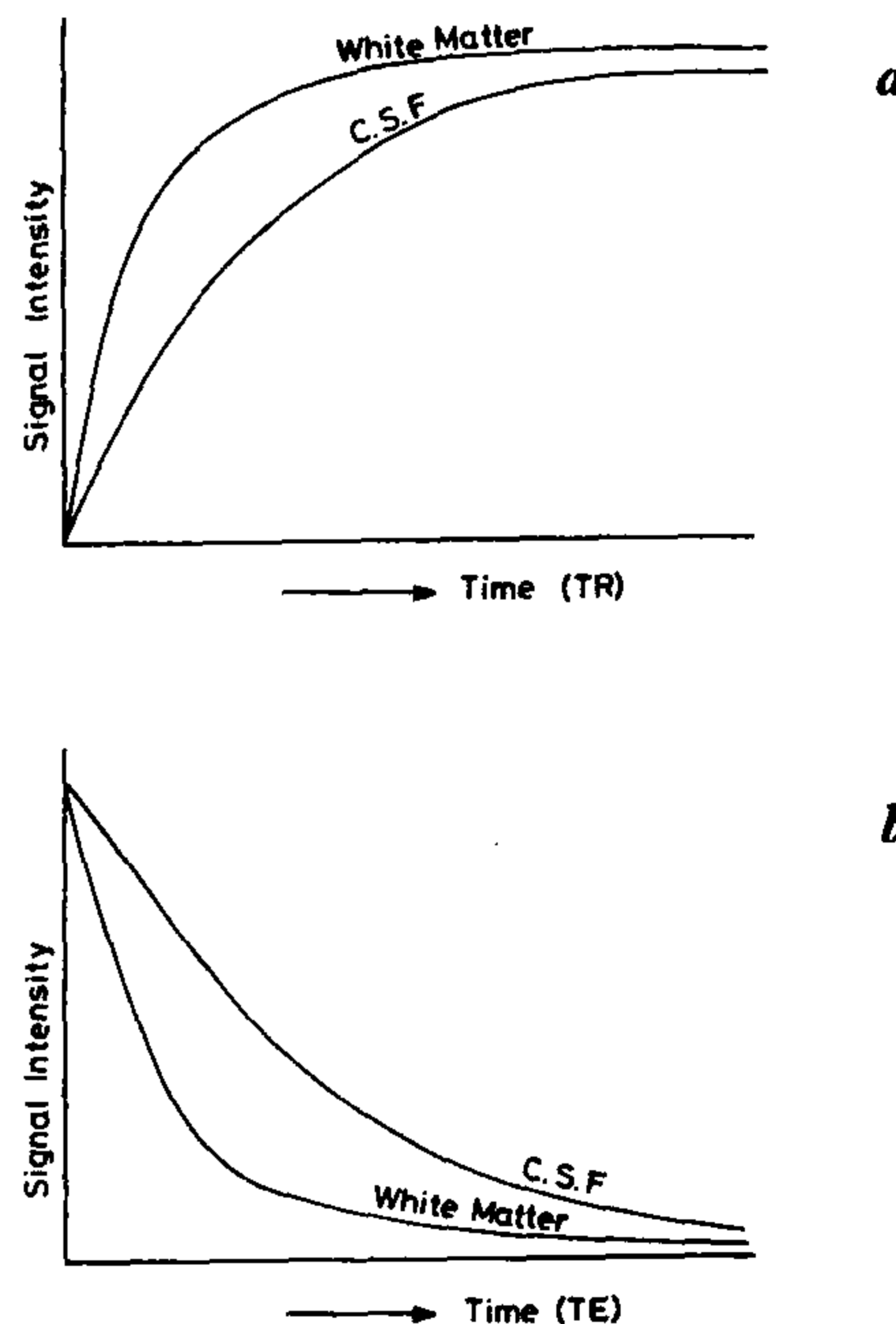


**Figure 6.** Relative MR signal intensities of two tissues (white matter and CSF) as a function of  $TR$  (a), and as a function of  $TE$  (b).

the pixel intensity in an MR image is a function of  $T_1$ ,  $T_2$ ,  $TE$  and  $TR$ . Generally, on  $T_1$ -weighted images, tissues with short  $T_1$  will appear bright and tissues with long  $T_1$  will appear dark. For example, in a  $T_1$ -weighted image of the brain, the fat will appear as white; white matter as light gray and gray matter as gray and the

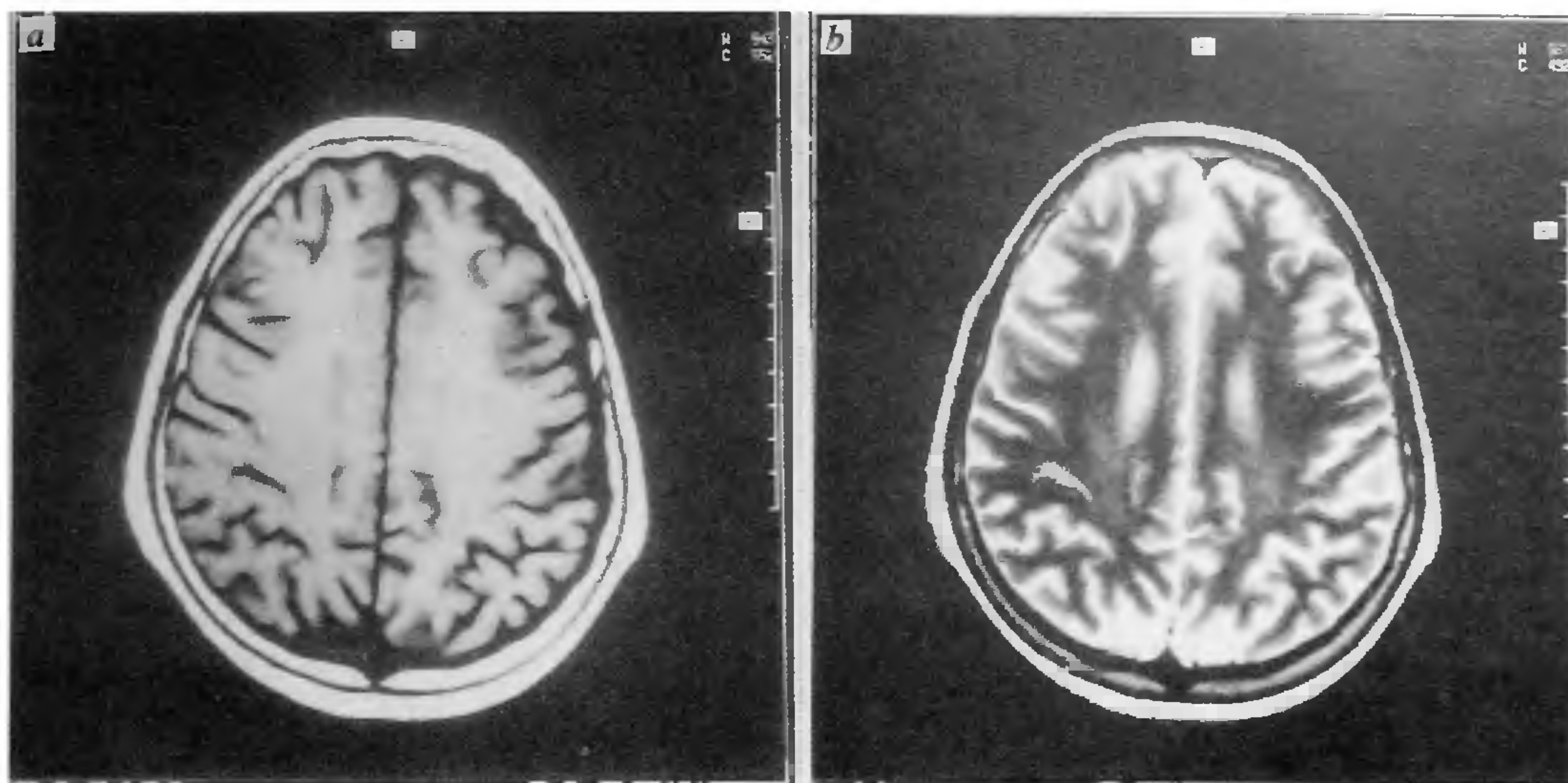


Figure 7a, b. Spin-echo images of the brain in the axial plane. *a*,  $T_1$ -weighted image acquired with a short  $TR$  (520 ms) and a short  $TE$  (15 ms), and *b*,  $T_2$ -weighted image acquired with a long  $TR$  (4500 ms) and a long  $TE$  (90 ms).

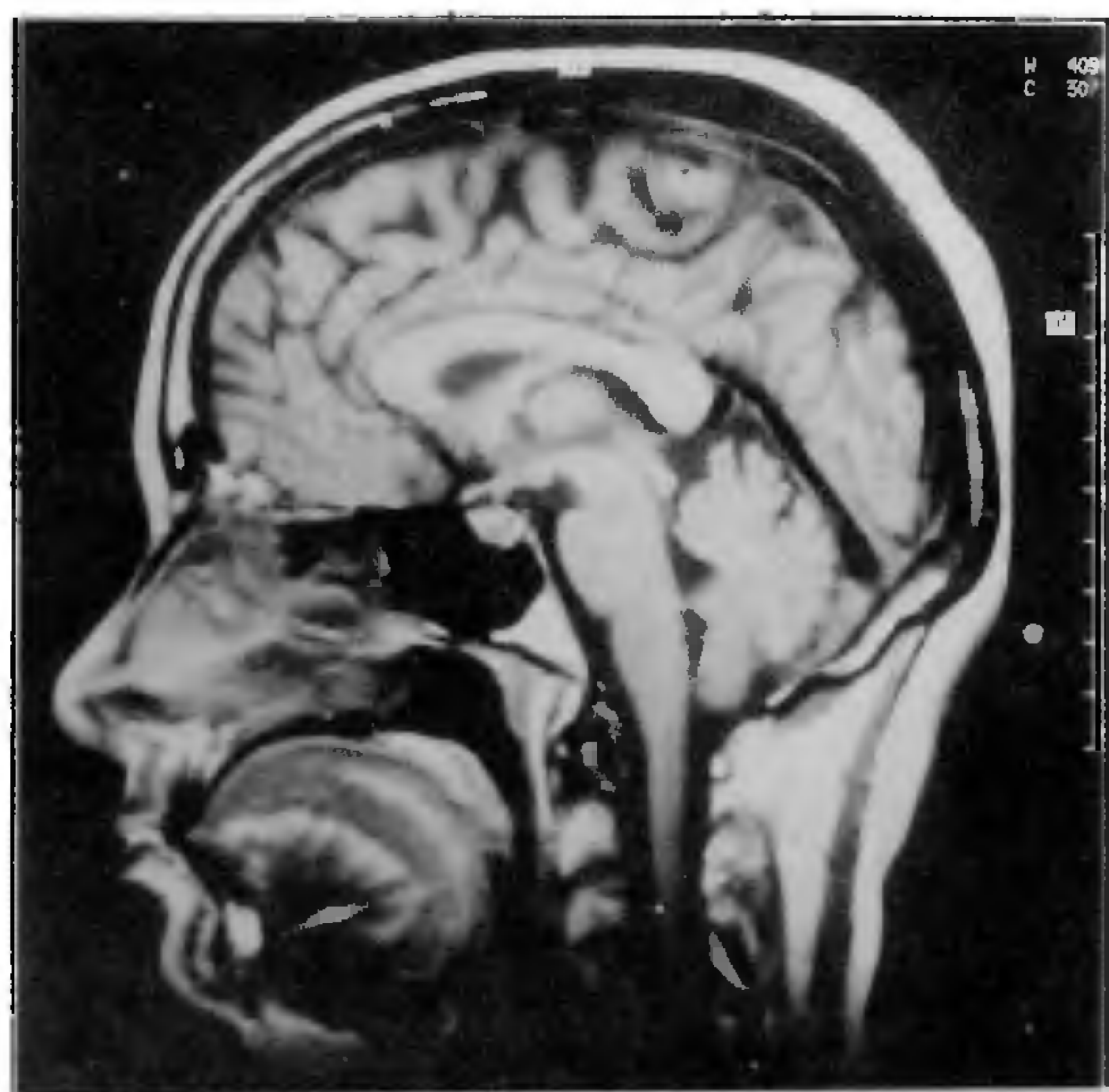


Figure 8. Spin-echo  $T_1$ -weighted mid-sagittal slice through the brain of a normal subject showing the different anatomical regions.

cerebrospinal fluid (CSF) as black (Figure 7a). In the  $T_2$ -weighted image of the brain, the fat appears as gray while the white matter as dark gray; the gray matter appears as gray and the CSF as white (Figure 7b). In general,  $T_1$ -weighted images are useful for viewing the anatomy, while  $T_2$ -weighted images are useful for identifying tissue pathology.



Figure 9. Axial  $T_2$ -weighted spin-echo image of a brain with tumour. The tumour is seen as a hyperintense region.

MRI is best suited for soft tissue diagnosis. Figure 8 is a sagittal MR image of the head and neck. The cerebral cortex, cerebellum, the lateral ventricles, pons, medulla, and the upper cervical cord are seen clearly. Bone, on the other hand, is invisible to this technique because



Figure 10. Sagittal spin-echo  $T_1$ -weighted image of the cervical spine, demonstrating a large disc protrusion causing compression of the spinal cord.

bone has only a few hydrogen atoms and the  $T_1$ s of their nuclear spins are too long in any case.

Details present in the MR image are far more than what are available with the best CT scanners. In fact, the MRI method differentiates best between white and gray matter within the brain (see Figure 8). It shows areas of demyelination in the brains of patients with multiple sclerosis with great sensitivity. The scans also discriminate between areas with varying blood flow, the picture intensity being proportional to the amount of blood flow. Accordingly, areas of ischaemia, large-vessel disease, or fast blood flow may be distinguished.

Most tumours and lesions in the central nervous system (CNS) have longer relaxation times,  $T_1$  and  $T_2$ , compared with values for normal tissue from similar regions. Brain pathology is best demonstrated with late echoes, using long  $TE$  values ( $T_2$ -weighted image), as illustrated in Figure 9. Tumours, infarction, haemorrhage, and demyelinating diseases show good contrast in such  $T_2$ -weighted images<sup>15,25,26</sup>. Many abnormalities of the spine are well documented in MR images, such as slipped disk. Diseases of the spinal cord are best defined by sagittal plane MR images<sup>27</sup> (Figure 10).

MRI has wide applications in the musculoskeletal system<sup>28,29</sup> as well. Fat, muscle fibrous structures, nerves and blood vessels have different MR image characteristics. MRI is excellent for evaluating the knee for internal derangement, such as meniscal and ligamentous

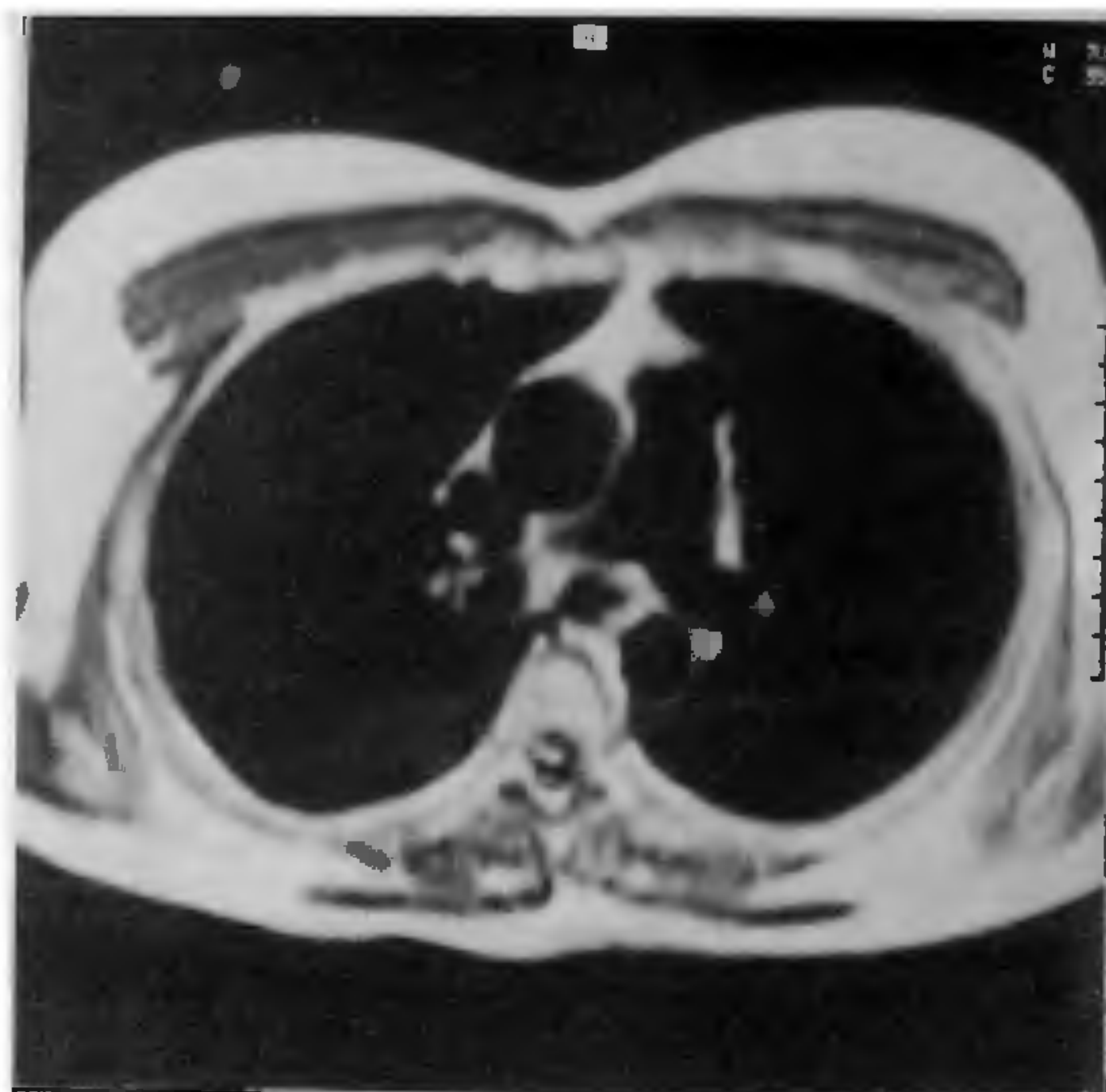


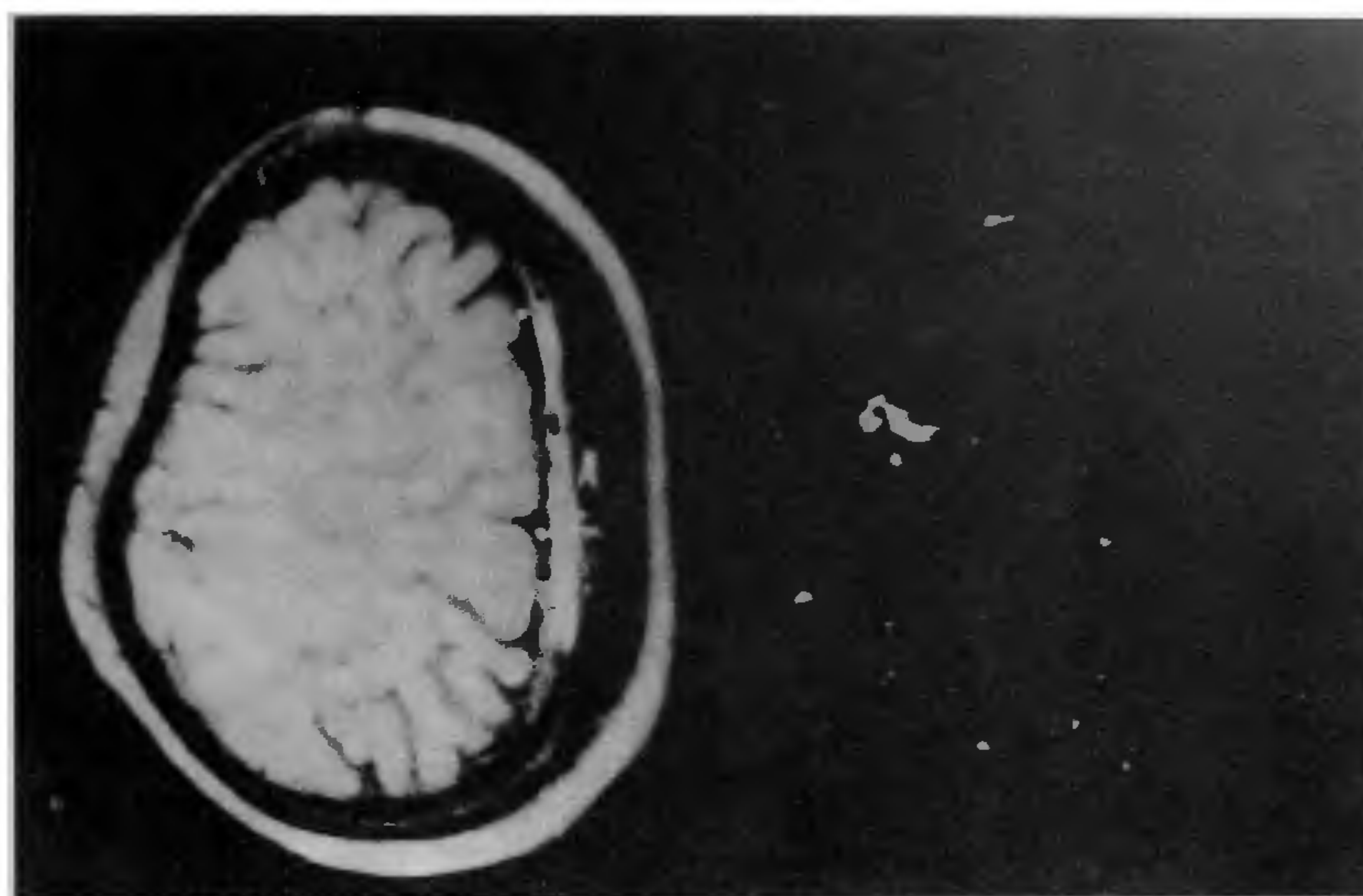
Figure 11. Axial spin-echo  $T_1$ -weighted ECG gated cardiac image through the chest and heart from a normal subject.



Figure 12. MR angiography demonstrating the arterial vessels in the head.

injuries. This imaging modality is not only valuable in hip-imaging, but is also extremely useful in the assessment of vascular necrosis, bone marrow diseases, osteomyelitis, osteoporosis, joint effusion, etc.

Recently, cardiovascular MRI has emerged as a new subspecialty<sup>30</sup>. It is useful for detecting most congenital cardiac abnormalities such as acute myocardial ischaemia-



**Figure 13.** Functional MR image (fMRI) from a study of task activation. Anatomy of the selected plane is shown on the left while the effects of activation (due to left-hand movement) is shown on the right.

mia, infarction and coronary artery diseases, and for evaluating bypass grafts, etc. The axial plane (Figure 11) is useful for visualization of the heart chambers and the aorta, etc. while the coronal view offers a more familiar anatomic representation of the heart and vessels. Cardiac images are best obtained using ECG-gated triggering or pulse triggering to avoid artifacts due to the heart motion. It is possible to get either images of multiple consecutive slices throughout a cardiac cycle, or multiple images of the same slice to accumulate functional information about blood flow and myocardial activity<sup>30</sup>. MR images can also be put in 'cine-display' mode in the computer's memory to obtain a motion picture of the heart simulating real-time conditions, thus enabling the assessment of cardiac functions in patients with valvular lesions.

Magnetic resonance angiography (MRA) is yet another ramification of the imaging technique which has proved its worth in evaluating vascular diseases<sup>31</sup>. It is based on methods to generate signal from moving spins (blood) while suppressing signal from stationary spins (the rest of the soft tissue), as shown in Figure 12. MRA is useful for diagnosing vascular pathology, such as cardiac abnormalities<sup>30</sup>, circulatory changes and chronic diseases of the liver<sup>32</sup>, renal blood flow, pulmonary embolism<sup>33</sup>, atherosclerosis, occlusive disease of lower extremity<sup>34</sup>, etc.

Recent developments in MRI methodology have demonstrated the possibility of observing<sup>26,35,36</sup> human brain functions through functional MRI (fMRI). This tech-

nique has great potential for assessing individual pathophysiology and for characterizing human brain functions such as language-learning, memory, task activation, etc. Figure 13 shows the effect of left hand movement performed by a volunteer; the appropriate cortical activity can be clearly seen near the sulcal wall. More details of functional MRI images have been published by us recently<sup>37</sup>.

Since ionizing radiation is absent, the technique is judged to have no adverse effects on the patients being scanned. However, such considerations as the safety of MRI scanning in pregnant women need to be more fully evaluated. Nevertheless, it is presently felt that the use of MRI will be determined more by (cost : benefit) considerations rather than by (risk : benefit) decisions.

### Future expectations

Improvements in MRI scanners will result in increased resolution, namely, more accurate localization and measurement of larger number of points in a given area (pixel) or volume (voxel). Several further offshoots of the scanning technique are available, of which 'metabolite imaging' offers a tremendous diagnostic potential<sup>26</sup>. Since the resolution of fast MRI techniques such as EPI is so good, brain cell groups 1 mm apart can be readily distinguished, and many fascinating brain functions such as dream state, schizophrenia, epilepsy, etc. can be understood noninvasively.

Other promising MRI techniques such as magnetization transfer, diffusion imaging, application of new contrast agents, and perfusion imaging have great promise for disease diagnosis as well.

## Conclusions

Magnetic resonance imaging is an exciting new technique for noninvasively probing the human body at three distinct levels of investigation, viz. gross or morphological anatomy, metabolite-level imaging, and functional imaging. MRI promises to supply information about physiologic processes within the body by relatively safe, and certainly very fast, methods. In doing so, it may substantially improve our understanding of the functioning of body tissues and fluids in normal and in diseased states.

1. Purcell, E. M., Torrey, H. C. and Pound, R. V., *Phys. Rev.*, 1946, **69**, 37-38.
2. Bloch, F., *Phys. Rev.*, 1946, **70**, 460-474.
3. Bloch, F., Hansen, W. W. and Packard, M., *Phys. Rev.*, 1946, **70**, 474-485.
4. Jackson, J. A. and Langham, W. H., *Rev. Sci. Instrum.*, 1968, **39**, 510-513.
5. Cooke, R. and Wien, R., *Biophys. J.*, 1971, **11**, 1002-1017.
6. Hansen, J. R., *Nature*, 1971, **230**, 482-486.
7. Hazlewood, C. F., Nichols, B. L., Chang, D. C. and Brown, B., *Johns Hopkins Med. J.*, 1971, **128**, 117-131.
8. Damadian, R., *Science*, 1971, **171**, 1151-1153.
9. Hollis, D. P. and Saryan, L. A., *Johns Hopkins Med. J.*, 1972, **131**, 441-444.
10. Weisman, I. D., Bennett, L. H., Maxwell, L. R., Woods, M. W. and Burke, D., *Science*, 1972, **178**, 1288-1290.
11. Lauterbur, P. C., *Nature*, 1973, **242**, 190-191.
12. Mansfield, P. and Morris, P. G., *NMR Imaging in Biomedicine*, Academic Press, New York, 1982.
13. Morris, P. G., *Nuclear Magnetic Resonance Imaging in Medicine and Biology*, Clarendon, Oxford, 1985.
14. Gadian, D. G., *NMR and its Application to Living Systems*, Clarendon, Oxford, 1982.
15. Stark, D. and Bradley, W. (eds), *Magnetic Resonance Imaging*, Moseby Company, St. Louis, 1992, 2nd edn.
16. Shaw, D., *Fourier Transform NMR Spectroscopy*, Elsevier, Amsterdam, 1984.

17. Kumar, A., Welte, D. and Ernst, R. R., *J. Magn. Reson.*, 1975, **18**, 69-83.
18. Ernst, R. R., Bodenhausen, G. and Wokaun, A., *Principles of Nuclear Magnetic Resonance in One and Two Dimensions*, Clarendon, Oxford, 1987.
19. Haase, A., Frahm, J., Hanicke, W., Merboldt, K. D. and Matthaei, D., *J. Magn. Reson.*, 1986, **67**, 258-266.
20. Leifer, M. C. and Willey, B. P., *Abstracts SMRM (London)*, 1985, p. 1013.
21. Hennig, J., Neurath, A. and Freiburg, H., *Magn. Reson. Med.*, 1986, **3**, 823-833.
22. Mansfield, P., *J. Phys. C: Solid State Phys.*, 1977, **10**, L55-57.
23. Wehrli, F. W., *Fast Scan Magnetic Resonance (Principles and Applications)*, Raven Press, New York, 1991.
24. Sauter, R., Schneider, M., Wicklow, K. and Kolem, H., *Electromedica*, 1992, **60**, 32-54.
25. De Certaines, J. D., Bovee, W. M. M. J. and Podo, F. (eds), *Magnetic Resonance Spectroscopy in Biology and Medicine: Functional and Pathological Tissue Characterization*, Pergamon Press, Oxford, 1992.
26. Kucharczyk, J., Moseley, M. and Barkovich, A. J. (eds), *Magnetic Resonance Neuroimaging*, CRC Press, Boca Raton, 1994.
27. Maney, C. (ed), *Imaging of the Spine and Spinal Cord*, Raven Press, New York, 1992.
28. Beltran, J., *MRI of Musculoskeletal System*, J. P. Lippincott Co., Philadelphia, 1990.
29. Descheppe, A. M. A. and Degryse, H. R. M., *MRI of Bone and Soft Tissue Tumors and their Mimics*, Kluwer, London, 1991.
30. Vander Wall, E. E. and De Ross, A. (eds), *Magnetic Resonance Imaging in Coronary Artery Disease*, Kluwer, Boston, 1993.
31. Dumoulin, C. L., *Radiology*, 1986, **161**, 717-720.
32. Burkart, D. J., Johnson, C. D., Morton, M. J. and Ehman, R. L., *Radiology*, 1993, **187**, 407-412.
33. Grist, J. M., Sostman, J. R., Macfall, J. R., Foo, T. K., Spritzer, C. E., Witty, L., Newman, G. E., Debrain, J. F., Tapson, V. and Saltzman, H. A., *Radiology*, 1993, **189**, 523-530.
34. Yucal, E. K., Kaufman, J. A., Geller, S. C. and Waltman, A. C., *Radiology*, 1993, **187**, 637-641.
35. Belliveau, J. W., Kennedy, D. N., McKinsty, R. C., Buchbinder, B. R., Weisskoff, R. M., Cohen, M. S., Vevea, J. M., Brady, T. J. and Ross, B. R., *Science*, 1991, **254**, 716-719.
36. Connelly, A., Jackson, G. D., Fracknowiak, R. S., Belliveau, J. W., Vargha-Khadem, F. and Gadian, D. G., *Radiology*, 1993, **188**, 125-130.
37. Jagannathan, N. R. and Raghunathan, P., *Curr. Sci.*, 1995, **69**, 448-451.

**ACKNOWLEDGEMENTS.** Financial support from the Department of Science and Technology, Government of India and Department of Biotechnology, Government of India in the initial acquisition of MRI equipment is gratefully acknowledged.